Journal of Thermal Science Vol.31, No.5 (2022) 1723−1733

**https://doi.org/10.1007/s11630-020-1382-3** **Article ID: 1003-2169(2022)05-1723-11**

# Flow Control Effect of Spanwise Distributed Pulsed Arc Discharge Plasma Actuation on Supersonic Compressor Cascade Flow

**SHENG Jiaming[1], WU Yun[1,2], ZHANG Haideng[1,2*], WANG Yizhou[1], TANG Mengxiao[1]**

1 Science and Technology on Plasma Dynamic Laboratory, Air Force Engineering University, Xi'an 710038, China
2 Institute of Aero-engine, School of Mechanical Engineering, Xi'an Jiaotong University, Xi'an 710049, China



**Abstract:** To achieve efficient control of supersonic compressor cascade flow, a type of spanwise distributed pulsed arc discharge plasma actuation (PADPA) was designed. To simulate the influences of PADPA on the flow field, a phenomenological model was established. Then, the flow control effects of PADPA on supersonic compressor cascade flow were researched numerically. The results show that under low static pressure ratio condition, the compressive wave induced by PADPA reduced the intensity of the passage shock wave, which eventually reduced shock wave loss. It was also found that PADPA produced an adverse pressure gradient (pre-compression effect) around the actuation location, which reduced the strength of the high adverse pressure gradient induced by the passage shock wave. The airflow on both sides of the actuation location was accelerated by PADPA owing to the spanwise distributed layout. Thus, it improved the ability of the boundary layer to resist the effect of the adverse pressure gradient and reduced the separation zone. Consequently, the total pressure loss was reduced by 6.8%. Under high pressure ratio condition, the effect of PADPA on the suction side controlling the large separation of the boundary layer was insignificant. The total pressure loss also increased slightly.

**Keywords: plasma, flow control, supersonic cascade, shock wave/boundary layer interaction, numerical simulation**

## 1. Introduction

With the continuous development of technology, the aircraft engine rotating speed and the flow velocity relative to the blades continue to increase, even reaching transonic or supersonic speed. Under supersonic inlet conditions, the static pressure increases owing to the shock wave structure arising in the blade passage. However, certain new problems have been encountered while applying this method. First, as the rotational speed of the compressor and intensity of the shock wave continue to increase, shock wave loss becomes larger. Second, because of the interaction between the shock wave and boundary layer, the boundary layer separates under a strong adverse pressure gradient, resulting in an increase in viscosity loss [1]. Third, the shock wave/boundary layer interaction induces low-frequency shock wave oscillation. Then, the low-frequency oscillation of aerodynamic load will lead to vibration of the mechanical structure which might endanger flight safety [2]. Therefore, it is important to effectively solve the problem of shock wave/boundary layer interaction in supersonic compressor.

Various studies of supersonic compressor flow control have been conducted to solve the problem of shock wave/boundary layer interaction. Flow control methods

Received: Jun 09, 2020 AE: KAN Xiaoxu Corresponding author: ZHANG Haideng E-mail: zhanghaideng@126.com

**Nomenclature**

| | | | |
|---|---|---|---|
| $C$ | chord/mm | $x, y, z$ | cartesian coordinates/mm |
| $f$ | actuation frequency/Hz | **Greek symbols** | |
| $L$ | distance/mm | $\beta$ | angle/(°) |
| $l$ | arc length/mm | $\eta$ | heat efficiency of discharge |
| $P$ | pressure/Pa | $\rho$ | density/kg·m$^{-3}$ |
| $Q$ | the single pulsed arc discharge energy/J | $\sigma$ | solidity |
| $q$ | space heating power/W·m$^{-3}$ | $\tau$ | the single pulse discharge deposition time/s |
| $r$ | radius of the discharge zone/mm | $\omega$ | total pressure loss coefficient |
| $s$ | pitch/mm | **Subscripts** | |
| $t$ | flow time/s | 0 | discharge center |
| $U$ | axial velocity/m·s$^{-1}$ | 1 | inlet plane |
| $V$ | the discharge area volume/m$^3$ | 2 | local location |

include passive and active controls. In passive control methods, the vortex generator [3] induces a pair of counter-rotating vortices, and the high momentum fluid in the mainstream is caught in the boundary layer. This can improve the velocity of the boundary layer and inhibit the shockwave-induced boundary layer separation. Bump control [4] reduces the flow loss of transonic compressor blades and shockwave-induced separation by delaying and reducing the intensity of shock wave. The cavity covered perforated plate method [5] uses the gas flow inside the cavity to reduce the pressure jump on the impact surface and reduce the separation by arranging a porous cavity in the interaction zone between the shock wave and boundary layer. A perforated blade [6] uses the pressure difference between the suction side and the pressure side of the blade to generate a jet that generates vortices to promote boundary layer transition and improve the ability of the boundary layer to resist the strong adverse pressure gradient. The rough band [7] promotes the boundary layer transition in advance to avoid the large separation caused by the shock wave/laminar boundary layer interaction. In active control, the boundary layer suction [8] can effectively reduce the separation zone and flow loss. Passive control can produce satisfactory control effects in design conditions and does not require addi- tional energy injection. However, the flight status of the aircraft is complicated; when it deviates from the designed working environment, passive control may be unable to achieve satisfactory control effect or even increase drag or separation and reduce performance.

Plasma flow control is a typical active control technology with the advantages of opening and closing at any time, simple structure, and quick response. This technology is applied to the low-speed flow control field, supersonic flow control field, and hypersonic field. Typical plasma actuation methods include dielectric barrier discharge (DBD), plasma synthesis jet actuation (PSJA), and arc discharge plasma actuation (ADPA) [9]. At present, various researchers have chosen dielectric barrier discharge plasma actuation to control the internal flow of the compressor.

Different studies have been conducted to investigate a large number of topics related to DBD controls of the internal flow of the compressor. DBD has the function of suppressing the corner separation of the compressor cascade [10, 11], improving the compressor stall margin [12, 13], reducing the leakage vortex strength [14], regulating the flow of the compressor cascade boundary layer and reducing the flow loss [15], reducing blade vibration load, and expanding the flutter boundary of the compressor blade [16].

Pulsed arc discharge plasma actuation (PADPA) is a typical plasma flow control method that uses plasma generated by a pulsed arc plasma actuator to control the flow. PADPA is dominated by Joule thermal effects and has the characteristics of large energy deposition. At present, PADPA has achieved remarkable control effects in shock wave/boundary layer interaction control, such as reducing shock wave drag and promoting mixing. Ref. [17] adopted an array-type PADPA to control the compression ramp shock wave/boundary layer inter- action and found that the control gas blobs (CGBs) generated by PADPA can diverge the shock waves and reduce the intensity of oblique shock as well as adverse pressure gradient when the CGBs pass through shock waves. Ref. [18] applied a stable DC arc discharge plasma actuation upstream of a spherical blunt body and found that the heat injected by the arc plasma is similar to the solid spike, which can change the shape of the detached shock wave and reduce the shock wave drag. Ref. [19] found that the “direct mechanism” and “indirect

mechanism" of the interaction between the PADPA and the flow field have the effect of promoting mixing. Therefore, it can be concluded that the adoption of arc plasma actuation for controlling the internal flow of the supersonic compressor is feasible using the control mechanism. To develop an efficient flow control method for the internal flow of supersonic compressor, the typical pre-compression supersonic compressor cascade ARL-SL19 was adopted as the research object, and a three-dimensional pulsed arc discharge plasma heat source model was established. Three-dimensional unsteady Reynolds-averaged Navier-Stokes (RANS) numerical simulation was used as a research tool to study the mechanisms of PADPA flow control of the supersonic cascade. The mechanism of PADPA for reducing shock wave intensity and shock wave/boundary layer interaction induced separation was revealed. These results can provide a new idea for flow separation control and loss reduction of supersonic compressor.

## 2. Establishment of Simulation Model

### 2.1 Establishing the PADPA heat source model

The arc discharge process involves very complex chemical reactions and complex physical phenomena such as the movement of charged particles in the electric field. PADPA uses the heat effect generated by its discharge and the shock wave generated by the energy deposition to control the flow field. Therefore, it is reasonable to equate the energy deposition generated by arc discharge to Joule heating. Joule heating is the result of moving charged particles that are randomly colliding and converting part of their kinetic energy into thermal energy. To simulate the Joule heating effect generated by PADPA, this study simplified it as a pure heat source model, established a power density model, and then added the power density to the Navier-Stokes equation. The simplified pure heat source model does not focus on the details of discharges such as chemical reactions and the movement of charged particles. It only focuses on the direct effect of the actuation on the flow field and couples the actuation into the fluid equation in the form of heat source terms. Good simulation results were obtained from the simplified model [20].

According to the results of the electrical parameters of pulse arc discharge plasma in Ref. [21], the single pulsed arc discharge energy was fixed at 30 mJ. According to Ref. [22], the heat conversion rate of pulse discharge was approximately 35%. Thus, the heat injection of a single pulsed arc discharge was approximately 10.5 mJ. To simplify the heat source model, PADPA was considered as a uniform discharge form in space and time, and the discharge zone was considered to have a semi-cylindrical shape. The space heating power $q(x, y, z, t)$ is as follows:

$$q(x,y,z,t)=\begin{cases}\dfrac{\eta Q}{\tau V}, \text{when}\left(x-x_0\right)^2+\left(y-y_0\right)^2\le r^2,\ z_0-\dfrac{l}{2}\le z\le z_0+\dfrac{l}{2},\ \text{and}\ 0\le t\le\tau\\ 0, \text{others}\end{cases} \tag{1}$$

where $x$, $y$, $z$ is cartesian coordinates; $t$ is flow time; $\eta$ is heat efficiency of discharge; $x_0$ and $y_0$ are the coordinates of the center point of the wall surface in the discharge zone; $r$ is the radius of the discharge zone; $V$ is the discharge area volume; $\tau$ is the deposition time of the single pulse discharge; $Q$ is the single pulsed arc discharge energy.

According to the arc discharge image captured by a high-speed camera in Ref. [23], the arc discharge zone is estimated to be 5 mm×2 mm×5 mm. In this study, $r$ was set as 1.6 mm, and the energy deposition time $\tau$ was set to 1 μs. The distance between the actuator electrodes, arc length $l$ was set to 5 mm.

To verify whether the heat source model could simulate the characteristics of PADPA, this study carried out a numerical simulation of the model under a static environment with 0.02 MPa pressure and compared it with experimental results. The experimental results were carried out using a high-speed schlieren system.

The schlieren diagrams of the numerical and experimental schlieren at different moments are shown in Fig. 1. By comparing the experimental schlieren results with the simulation results, the shape size of the thermal deposition zone and the shock wave patterns of the simulation results were in good agreement with the experimental results.

### 2.2 PADPA layouts

The ARL-SL19 supersonic cascade has a higher intensity of normal shock wave when the static pressure ratio is 2.12. Therefore, the interaction between the shock wave and pressure side boundary layer forms a large separation leading to separation loss. When the static pressure ratio is 2.40, the normal shock wave moves forward in the passage, causing a decreased Mach number in front of the normal shock wave, which reduces the shock wave intensity and causes the separation zone disappear, and there is a large separation on the suction side. According to the previous experiment and simulation studies on the plasma control compression ramp shock wave/boundary layer interaction, arranging the PADPA upstream of the interaction zone of the shock wave and boundary layer is better. Therefore, in low static pressure ratio conditions, this study applied PADPA

in front of the pressure side shock wave/boundary layer interaction zone. Under high static pressure ratio conditions, PADPA was applied in front of the suction side shock wave/boundary layer interaction zone. A schematic diagram of the PADPA layout is shown in Fig. 2, where Fig. 2(a) is a top view; Fig. 2(b) is a front view at the static pressure ratio of 2.12, and Fig. 2(c) is a front view at the static pressure ratio of 2.40. The layout is a spanwise distributed method. The actuators are arranged at intervals along the blade radial direction. The blade

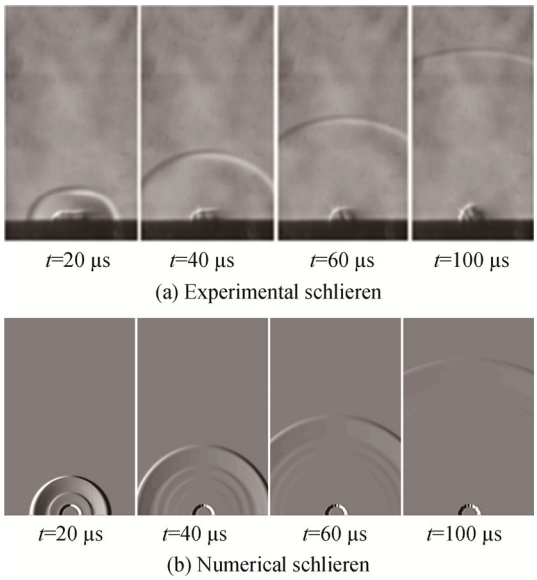


**Fig. 1** Schlieren diagrams of experimental and numerical results

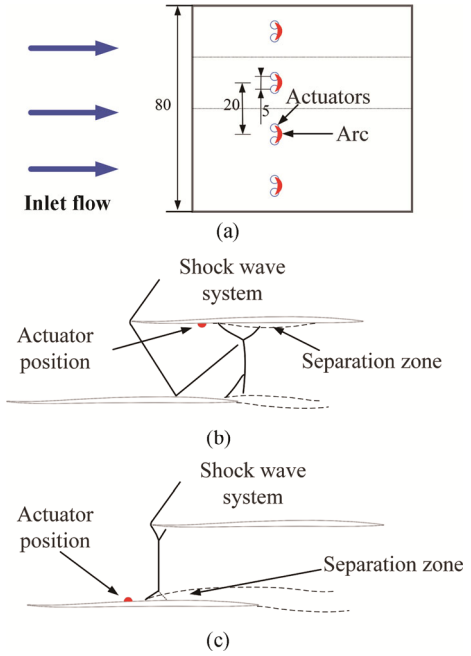


**Fig. 2** Schematic of PADPA layout

width is 80 mm, and four actuators are arranged at equal intervals along the blade radial direction. The distance between each actuator is 20 mm, and the distance between each actuator electrode is 5 mm. Through this actuator layout method, the whole blade flow field is fully covered by the actuators. Furthermore, according to previous research, it is found that the pulsed arc discharge heat energy injected into the flow field had a thermal blockage effect. If spanwise connected layout method was used, the strong blocking effect would lead to early separation and significantly increase separation loss. On the one hand, the distributed layout method could reduce the thermal blockage problem. On the other hand, the spanwise connected layout method will require more energy.

### 2.3 Cascade calculation model

A typical supersonic precompression blade ARL-SL19 was adopted as the research object. The profile shape coordinates and main design parameters of the blade are obtained as per instructions in Ref. [24]. Table 1 lists the main design parameters of ARL-SL19.

**Table 1** Main design parameters of ARL-SL19 [24]

| Parameters | Symbols | Values |
|---|---|---|
| Chord | $C$/mm | 85 |
| Pitch | $s$/mm | 55.58 |
| Solidity | $\sigma$ | 1.53 |
| Stagger angle | $\beta_s$/(°) | 56.93 |

Calculations were carried out using Fluent v16, and the density-based implicit method was used to solve the three-dimensional transient N-S equation. The inlet boundary condition was set as supersonic inlet pressure far-field, and the total inlet temperature, total pressure and velocity components in all directions were provided. The outlet boundary condition was set as the pressure outlet, and the outlet static pressure was provided. The periodic boundary condition was set as the translational periodic boundary condition. The blade wall was set as the non-slip adiabatic wall boundary condition.

### 2.4 Sensitivity analysis of the grid size and turbulence model selection

H-shaped structured grids with hexahedral elements and an O-grid around the airfoil were used for the validation study and grid sensitivity analysis. To ensure the full development of airflow, the inlet boundary was placed 230% of the axial chord upstream of the leading edge, and the outlet boundary was approximately 240% of the axial chord downstream of the trailing edge. To avoid reflection at the boundary, a buffer region was imposed and the outlet boundary was set to no reflection

boundary condition. The cascade grid is shown in Fig. 3. The first layer height at the wall was set to 0.001 mm to ensure $y^+<1$. The distances of two plasma actuators layout along the blade radial direction were 20 mm. Thus, to reduce the amount of calculations, we selected one of the cycles for numerical simulation, which is shown by the dotted lines in Fig. 2(a). Both ends of the blade were set as symmetrical boundary conditions. In this H-shaped structured grid, the grids along the $X$, $Y$, and $Z$ directions were densified and the number of nodes of the three grid settings was 300×90×30, 350×110×40, and 400×140×56, respectively.

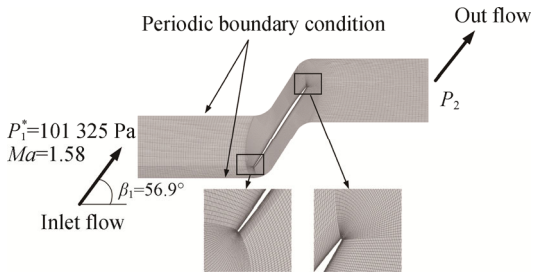


**Fig. 3** Blade passage grid

According to the experimental condition (static pressure ratio of 2.3), the numerical simulation was performed and compared with the experimental results. In this numerical simulation, the inlet total pressure was set as 101 325 Pa; the inlet Mach number was set as 1.58; the inlet angle was 56.9°; the outlet static pressure was set as 56 474 Pa, and the simulation time step was set as 100 ns. Because the inlet flow was supersonic and the temperature increased when the plasma was applied, the viscosity could not be considered constant. Sutherland's law was used to regulate the viscosity with temperature.

To analyze the influence of the turbulence model on the simulation results, four turbulence models are selected for simulation. Fig. 4 shows the isentropic Mach number on the blade surface of the four turbulence models when the static pressure ratio was 2.3. The simulation results show that the Shear-Stress Transport $k$-$\omega$ model gives the most accurate results. Hence the Shear-Stress Transport $k$-$\omega$ turbulence model was applied to simulate the flow field.

Fig. 5 shows the isentropic Mach number on the blade surface of the three grids settings when the static pressure

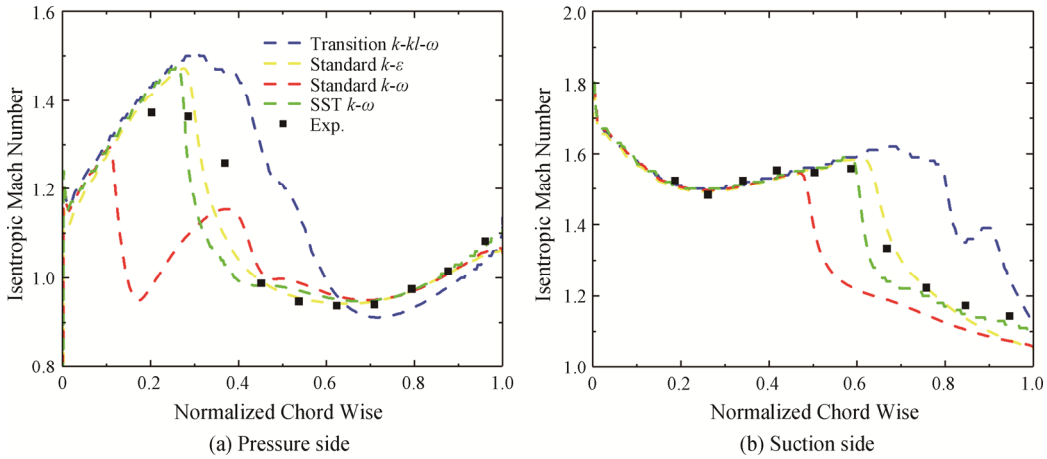


**Fig. 4** Isentropic Mach number on different turbulence models

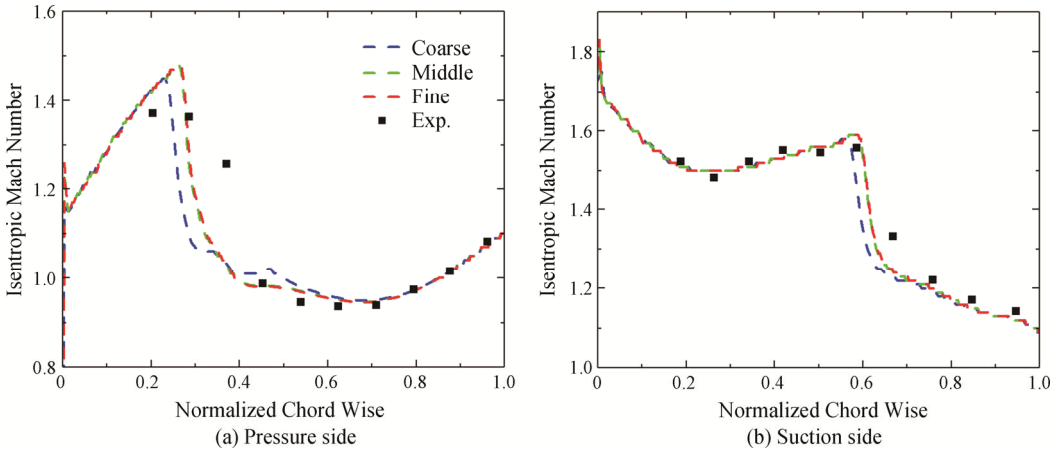


**Fig. 5** Isentropic Mach number on the blade surface

ratio is 2.3. According to the numerical simulation results and the experimental results, the suction side and the pressure side separation positions with the coarse grid was more forward than the medium grid and fine grid, and the isentropic Mach number deviated from the experimental results at the shock wave/boundary layer interaction zone. The medium grid and fine grid fit well with the experimental results. By weighing simulation accuracy and computational cost, the subsequent study used the medium grid.

## 3. Analysis of Simulation Calculation Results

The controllable parameters of PADPA include actuation frequency, single pulsed energy, discharge time, electrode spacing (affecting arc length), and electrode width (affecting arc thickness). We studied the effect of actuation frequency and single pulsed energy on the supersonic compressor cascade. There were eight numerical simulation conditions. By comparing the change in flow fields under different conditions, the effects of the actuation frequency and single pulsed energy on the supersonic cascade flow field structure were studied.

C_1 and C_6 are the baseline flow fields without actuation when the static pressure ratio is 2.12 and 2.40, respectively. C_2 to C_5 are four conditions with different actuation frequencies and energies when the static pressure ratio is 2.12, and actuations are applied at the position of 0.33 chord length on the pressure side. C_7 and C_8 are two conditions with different actuation frequencies when the static pressure ratio is 2.12, and actuations are applied at the position of the 0.32 chord length on the suction side. The detailed settings of each condition are listed in Table 2 (in which PS: Pressure side, SS: Suction side).

While the plasma actuation is imposed in the flow field, the simulation time step is 10 ns, and the simulation time step is changed to 100 ns after the plasma actuation is imposed to accelerate the simulation procedure.

**Table 2** Detailed settings of each condition

| Case | $q$/W·m$^{-3}$ | $f$/kHz | $L/C$ | Static pressure ratio |
|---|---|---|---|---|
| C_1 | 0 | 0 | – | 2.12 |
| C_2 | $1.0\times10^{11}$ | 20 | 0.33 (PS) | 2.12 |
| C_3 | $1.0\times10^{11}$ | 50 | 0.33 (PS) | 2.12 |
| C_4 | $5.0\times10^{11}$ | 20 | 0.33 (PS) | 2.12 |
| C_5 | $5.0\times10^{11}$ | 50 | 0.33 (PS) | 2.12 |
| C_6 | 0 | 0 | – | 2.40 |
| C_7 | $1.0\times10^{11}$ | 20 | 0.32 (SS) | 2.40 |
| C_8 | $1.0\times10^{11}$ | 50 | 0.32 (SS) | 2.40 |

### 3.1 Flow structure and loss analysis of baseline with low static pressure ratio

Fig. 6 shows the time-averaged Mach number contour diagram of the supersonic cascade when the static pressure ratio is 2.12. It can be seen from the figure that the supersonic cascade shock wave structures under this condition include the leading edge passage shock wave, the reflection shock wave, and the normal shock wave. The leading edge passage shock wave/boundary layer interaction leads to a small separation bubble structure on the suction side. Because the normal shock wave intensity is high, the normal shock wave/boundary layer interaction forms a large separation bubble structure on the pressure side.

To analyze the source of supersonic cascade loss and loss distribution, slices were made along the flow direction in the cascade passage. The contour diagram of the total pressure loss coefficient at each slice position was specified as well.

The total pressure loss coefficient can be defined as:

$$\omega = \frac{p_{t1} - p_{t2}}{p_{t1} - p_1} \tag{2}$$

where $p_{t1}$ is the incoming flow total pressure; $p_{t2}$ is the local total pressure; and $p_1$ is the incoming flow static pressure.

Fig. 7 shows the contour diagram of the cascade time-averaged total pressure loss distribution along the flow direction in the cascade passage. The results show

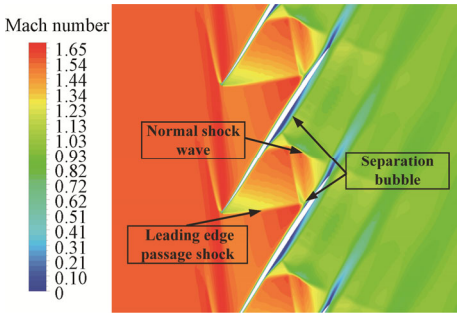


**Fig. 6** Time-averaged Mach number contour diagram of baseline flow when the static pressure ratio is 2.12

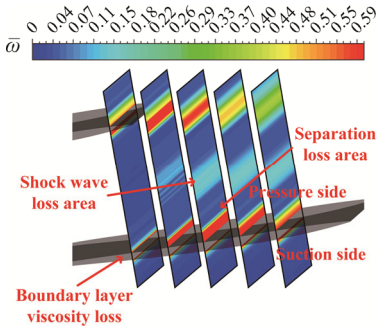


**Fig. 7** Contour diagram of cascade time-averaged total pressure loss distribution

that the main reasons for the supersonic cascade loss are the passage shock wave loss and boundary layer separation loss caused by shock wave/boundary layer interaction. In this condition, the pressure side flow loss is greater than that of the suction side. As can be seen from Fig. 6, the pressure side flow loss is mainly caused by the pressure side large separation.

### 3.2 Study on plasma actuation characteristics at low static pressure ratio

Fig. 8 shows the contour diagrams of the time-averaged total pressure loss coefficient under the C_2 to C_5 conditions. Fig. 8(a)–(d) show the C_2 to C_5 conditions sequentially. The detailed settings of each condition are listed in Table 2. The flow loss distribution changes significantly in the four conditions and the flow loss distribution near the pressure side shows a peak shape zone. Compared with the baseline flow field in Fig. 7, the flow loss is increased at the rear of the actuation location, and the flow loss on both sides of the actuation location is reduced to a certain extent. The energy deposition generated by PADPA leads to the thermal blockage effect. Therefore, the flow loss at the rear of the actuation location is increased to a certain extent. The reasons for the loss reduction on both sides of the actuation location will be further analyzed in later sections. In the four actuation conditions, the loss in the center of the passage is reduced. This was because of the compressive wave induced by PADPA that pre-compresses the airflow in front of the passage shock wave and reduces the shock wave intensity. In addition, the shock wave loss is reduced with an increase in the actuation frequency and energy. From Fig. 8(d), after high-energy and high-frequency actuation, the pressure side loss is significantly reduced, whereas the suction side loss is increased.

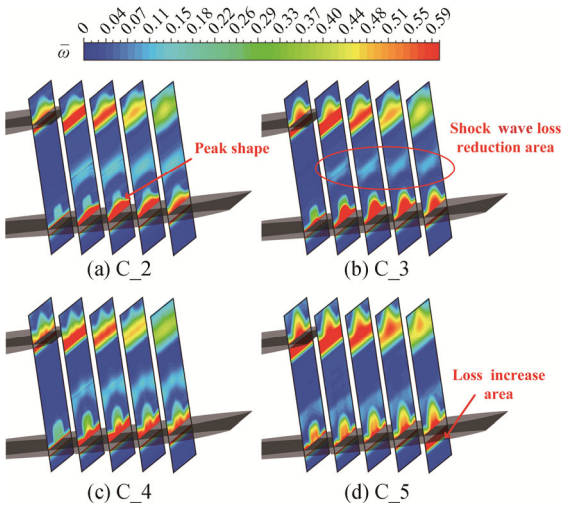


**Fig. 8** Contour diagram of the time-averaged total pressure loss coefficient in different conditions

To further explore the reasons for the significant loss reduction on both sides of the actuation location after applying actuation, the three-dimensional flow separation was shown by streamlines near the pressure side. Fig. 9 shows the time-averaged streamline on the pressure side in five conditions. For C_1, the separation zone appears as a uniform strip. After applying actuation, the separation zone shape changed and the uniformity is destroyed. For C_2 and C_3, the separation zone at the rear of the actuation location is extended, but the separation width is reduced. Even for C_3, the separation zone on both sides of the actuation location disappears. This illustrates that the direct reason for the loss reduction on both sides of the actuation location in Fig. 8 is the separation zone reduction.

For C_4, the separation zone at the rear of the actuation is contracted, and the separation zone on both sides of the actuation location is extended. The main reason is that the strong shock wave generated by the high-energy pulse actuation has a strong acceleration effect on the boundary layer and reduces the separation. For C_5, the blockage effect leads to the passage normal shock wave moving forward. As the Mach number in front of the shock wave decreases, the shock wave intensity is weakened and induces the contraction of the separation zone. It should be noted that although the pressure side separation is contracted in the high-energy and high-frequency actuation condition, the suction side flow loss is significantly increased, as shown in Fig. 8(d). This indicates that the suction side separation is extended owing to the shock wave moving forward.

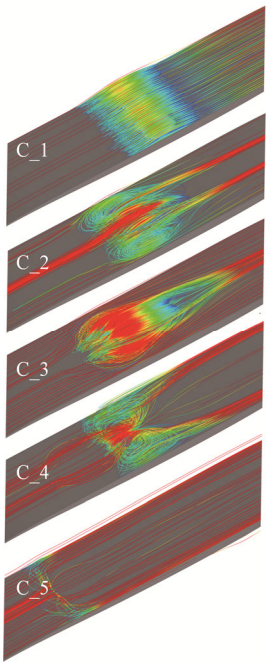


**Fig. 9** Time-averaged streamline on the pressure side

The contour diagrams of the pressure gradient on the pressure side are shown in Fig. 10. The pulsed arc discharge plasma actuation location is indicated by the black line frame. Fig. 10(a)–(e) indicate the C_1 to C_5 conditions sequentially. An adverse pressure gradient band on the pressure side is formed owing to the passage normal shock wave in the C_1 condition, which leads to serious separation problems on the pressure side. For C_2, C_3, and C_4, it is observed that after applying actuation, a bow pressure gradient band is formed on the wall. Concurrently, a favorable pressure gradient region appeared behind the arcuate pressure gradient band. The original straight shock wave is distorted owing to the upstream effect, and the shock wave moved forward in the middle of the blade. Comparing the strength of the pressure gradient, it can be observed that after applying actuation, the bow pressure gradient band pre-compresses the airflow on both sides of the actuation location and reduces the strong adverse pressure gradient. Therefore, it can be considered that the reason for the decrease in the separation zone or disappearance is PADPA causes a reduction in the adverse pressure gradient on both sides of the actuation location. For C_5, owing to the thermal blockage effect, the shock wave is pushed forward to the front of the actuation location, and the effect of reducing the adverse pressure gradient cannot be shown.

Fig. 11 shows C_3 condition time-averaged distribution of the limited streamlines on the pressure side. The pulsed arc discharge plasma actuation location is indicated by the white line frame. Due to the energy deposition, the thermal blockage effect causes the streamline near the wall deflecting to both sides of the actuation location. The airflow velocity on both sides is increased, which enhances the ability of the airflow to resist the adverse pressure gradient. In addition, it can be observed that a pair of reverse vortices are formed. The vortices promote the mixing of the mainstream with the boundary layer and can entrain the high-energy fluid of the mainstream zone into the boundary layer, which can increase the boundary layer energy to suppress shock wave induced separation. This effect is very similar to a vortex generator. It can be considered that the PADPA generates a virtual profile, which has a similar effect to the vortex generator. However, we should consider that the virtual profile generated by the thermal blockage is larger than the vortex generator and would cause flow loss.

To study the effect of PADPA on the overall performance of supersonic cascade, the time-averaged mass flow rate total pressure loss coefficient $\bar{\omega}$ is defined as:

$$\bar{\omega} = \frac{\iint \overline{p_{t1}\rho_1 U_1}\mathrm{d}s - \iint \overline{p_{t2}\rho_2 U_2}\mathrm{d}s}{\iint \left(\overline{p_{t1}\rho_1 U_1} - \overline{p_1\rho_1 U_1}\right)\mathrm{d}s} \tag{3}$$

where $p_{t1}$ is the incoming flow total pressure; $p_{t2}$ is the local total pressure; $p_1$ is the incoming flow static pressure; $\rho_1$ is the incoming density; $\rho_2$ is the local density; $U_1$ is the incoming axial velocity; $U_2$ is the local axial velocity, and the overline indicates the time-averaged result. The cross-section of the incoming flow parameter value was located at a 0.5 axial chord length upstream of the leading edge and the local flow parameter value cross-section was located at 0.56 axial chord length downstream of the trailing edge.

The time-averaged mass flow rate outlet flow angle $\overline{\beta_2}$ is defined as:

$$\overline{\beta_2} = \frac{\iint \overline{\beta_2\rho_2 U_2}\mathrm{d}s}{\iint \overline{\rho_2 U_2}\mathrm{d}s} \tag{4}$$

where $\beta_2$ is the outlet flow angle.

Fig. 12 shows a bar graph of the time-averaged mass flow rate total pressure loss coefficient at the outlet for each condition. The baseline total pressure loss coefficient is 12.20%. At the same actuation frequency of 20 kHz, the two different power conditions can increase flow loss, and the larger energy actuation condition has a greater loss. At the same actuation frequency of 50 kHz, the two different power conditions can reduce flow loss.

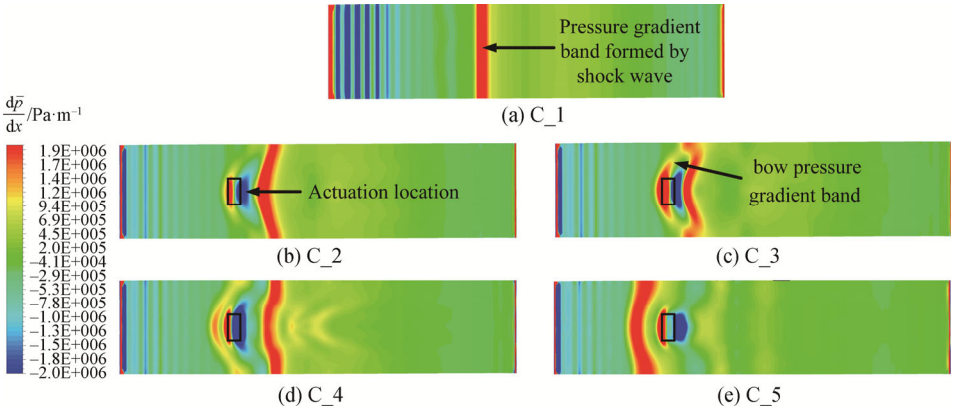


**Fig. 10** Contour diagram of pressure gradient on the pressure side

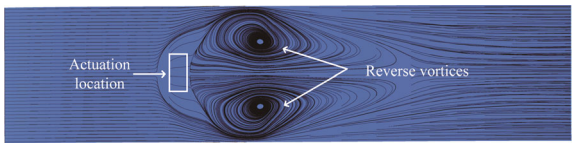


**Fig. 11** Distribution of the time-averaged limited streamline

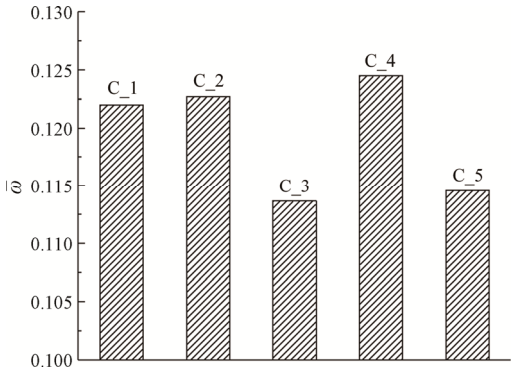


**Fig. 12** Bar graph of the time-averaged mass flow rate total pressure loss coefficient at the outlet

The C_3 condition loss is 11.37%, and the relative decline is 6.8%; the C_5 condition loss is 11.46%, and the relative decline is 6.1%. The loss of C_3 and C_5 is reduced, but the reasons for the loss reduction were different. From the above analysis, the strong blockage effect generated by high-frequency actuation with large energy causes the passage shock wave to move forward. Thus, the positive shock wave intensity is weakened, and the separation loss is also reduced.

The thermal blockage generated by the high-frequency actuation with low energy is not sufficient to move the shock wave forward, but the bow pressure gradient band generated by PADPA reduces the shock wave intensity on both sides of the actuation location, which leads to the disappearance of the separation. Based on the comprehensive analysis, it can be concluded that under this static pressure ratio, the flow control effect of low energy with high-frequency actuation to reduce the loss is better. The shock wave structure will not change significantly, and the energy consumption is also lower.

Fig. 13 shows a bar graph of the time-averaged mass flow rate outlet flow angle. The baseline outlet flow angle is 61.46°. It can be seen from the figure that the low energy discharge has no significant effect on the outlet flow angle, while the high energy discharge can reduce the outlet flow angle, and the higher the frequency of high energy discharge, the smaller the outlet flow angle.

### 3.3 Study on plasma actuation characteristics with the high static pressure ratio

Fig. 14 shows the time-averaged Mach number contour diagrams at different blade radial positions with a large static pressure ratio ($p_2/p_1$=2.40). Fig. 14(a) shows C_6 condition. Fig. 14(b) and (c) show Mach number contour diagrams at different blade radial positions ($Z$=10 mm and $Z$=18 mm, respectively) in the C_7 condition. Fig. 14(d) and (e) are the Mach number contours at different blade radial positions ($Z$=10 mm, $Z$=18 mm, respectively) in the C_8 condition.

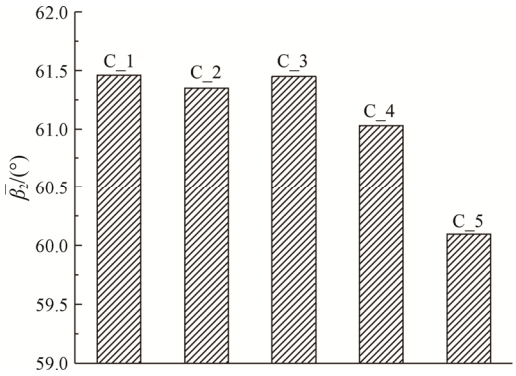


**Fig. 13** Bar graph of the time-averaged mass flow rate outlet flow angle

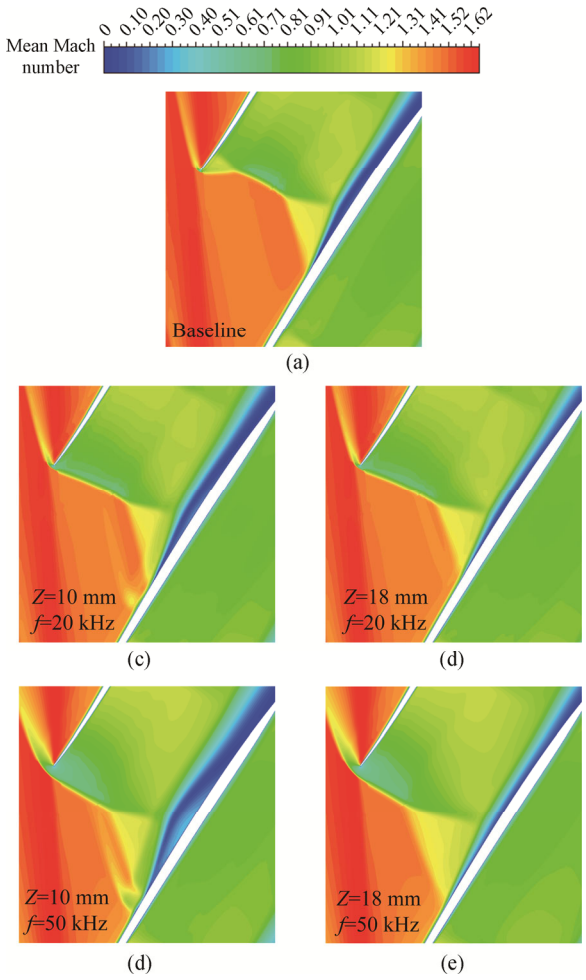


**Fig. 14** Time-averaged Mach number contour diagram at different blade radial positions on high static pressure ratio ($p_2/p_1$=2.40)

Fig. 15 shows the pressure gradient contour diagram of the suction side under the high-pressure rate condition ($p_2/p_1$=2.40). Fig. 15(a), (b), and (c) shows the C_6, C_7, and C_8 conditions, respectively. It can be seen from this figure that after applying actuation, the shock wave moves forward, and the higher the frequency, the more obvious the distance moved forward. Similar to applying actuation on the pressure side at a small static pressure ratio, the bow pressure gradient band generated in front of the passage shock wave weakens the shock wave intensity.

The above-mentioned method was used to calculate the baseline and actuation conditions. The values of $\bar{\omega}$ and $\overline{\beta_2}$ are listed in Table 3. It can be observed from the table that under the conditions of high static pressure ratio, the loss is slightly increased after applying actuation, and the outlet airflow angle does not change significantly. The main reason is that the separation zone on both sides of the actuation location is slightly contracted, but the separation zone at the rear of the actuation location is extended, which offsets the positive effect. The overall control effect is not high.

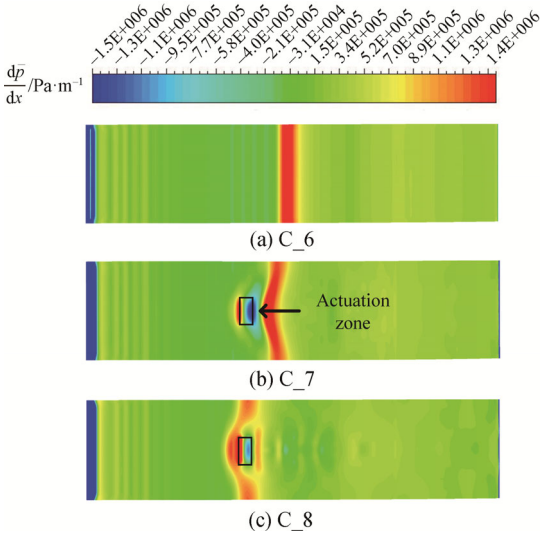


**Fig. 15** Contour diagram of pressure gradient on the suction side

**Table 3** $\bar{\omega}$ and $\overline{\beta_2}$ under different conditions at high static pressure rate

| Case | $\bar{\omega}$ | $\overline{\beta_2}$ |
|---|---|---|
| C_6 | 12.39% | 60.49 |
| C_7 | 12.59% | 60.39 |
| C_8 | 12.52% | 60.77 |

## 4. Conclusions

Based on the mechanism of pulsed arc discharge plasma actuation control on supersonic flow, a pulsed arc discharge plasma actuation heat source model was established. Considering the ARL-SL19 supersonic cascade as the research object, the three-dimensional transient RANS numerical simulation method was used to analyze the influence of frequency and single discharge energy on the supersonic cascade with spanwise distributed pulsed arc discharge plasma. The main conclusions include:

Spanwise distributed pulsed arc plasma actuation can induce a bow pressure gradient band and reduce the strong adverse pressure gradient caused by passage shock waves. The virtual profile formed by the actuation is comparable to a vortex generator that can generate a pair of reverse vortices, which accelerates the airflow on both sides of the actuation location and improves the ability of the airflow to resist the adverse pressure gradient. The thermal blockage caused by the actuation will also lead to separation expansion at the rear of the actuation location.

In the low static pressure ratio condition (i.e., when there is a strong passage normal shock wave), the high frequency with low energy actuation effect is better; the pressure side separation is significantly reduced, and the total pressure loss is reduced by 6.8%.

In the high static pressure ratio condition (i.e., when there is no strong passage normal shock wave), the separation on both sides of actuation location is decreased to some extent after applying actuation, but the positive effect is offset because of the increase in the separation at the rear of the actuation location. The control effect is not good.

## Acknowledgments

This research is supported by National Natural Science Foundation of China (Grant No. 51790511, 51906254).

## References

[1] Holger B., Shock wave boundary layer interactions. Cambridge University Press, New York, USA, 2011.

[2] Dolling D.S., Fifty years of shock-wave/ boundary-layer interaction research: what next? AIAA Journal, 2001, 39(8): 1517–1531.

[3] Panaras A.G., Lu F.K., Micro-vortex generators for shock wave/boundary layer interactions. Progress in Aerospace Sciences, 2015, 74: 16–47.

[4] John A., Qin N., Shahpar S., Using shock control bumps to improve transonic fan/compressor blade performance. Journal of Turbomachinery, 2019, 141(8): 081003.

[5] Yu S., Schnerr G.H., Dohrmann U., Passive control of shock-boundary layer interaction in transonic axial compressor cascade flow. Fluid- and Gasdynamics, 1994,

4: 207–217.

[6] Szwaba R., Comparison of the influence of different air-jet vortex generators on the separation region. Aerospace Science & Technology, 2011, 15(1): 45–52.

[7] Hergt A.S., Klinner J., Grund S., On the importance of transition control at transonic compressor blades. ASME Turbo Expo 2019, Phoenix, USA, GT2019-90440.

[8] Mao X., Liu B., Zhang G., Control of separations in a highly-loaded axial compressor cascade by tailored boundary layer suction. ASME Turbo Expo 2015, Montreal, Canada, GT2016-56795.

[9] Wu Y., Li Y.H., Progress and outlook of plasma flow control. Acta Aeronautica et Astronautica Sinica, 2015, 36(02): 381–405.

[10] Li Y.H., Wu Y., Zhou M., Control of the corner separation in a compressor cascade by steady and unsteady plasma aerodynamic actuation. Experiments in Fluids, 2010, 48(6): 1015–1023.

[11] Akcayoz E., Duc V.H., Mahallati A., Controlling corner stall separation with plasma actuators in a compressor cascade. Journal of Turbomachinery, 2016, 138(8): 081008.

[12] Zhang H.D., Wu Y., Yu X.J., Experimental investigation on the plasma flow control of axial compressor rotating stall. ASME Turbo Expo 2019, Phoenix, USA, GT2019-90609.

[13] Li G., Xu Y.J., Yang L.Y., Low speed axial compressor stall margin improvement by unsteady plasma actuation. Journal of Thermal Science, 2014, 23(2): 114–119.

[14] Zhang H.D., Wu Y., Li Y.H., Control of compressor tip leakage flow using plasma actuation. Aerospace Science and Technology, 2019, 86: 244–255.

[15] Zhang H.D., Wu Y., Li Y.H., Mechanism of compressor airfoil boundary layer flow control using nanosecond plasma actuation. International Journal of Heat and Fluid Flow, 2019, 80: 108502.

[16] Neumann P., De Almeida V.B., Motta V., Dynamic mode decomposition analysis of plasma aeroelastic control of airfoils in cascade. Journal of Fluids and Structures, 2020, 94: 102901.

[17] Gan T., Wu Y., Sun Z.Z., Shock wave boundary layer interaction controlled by surface arc plasma actuators. Physics of Fluids, 2018, 30(5): 055107.

[18] Schulein E., Zheltovodov A.A., Effects of steady flow heating by arc discharge upstream of non-slender bodies. Shock Waves, 2011, 21(4): 383–396.

[19] Firsov A.A., Savelkin K., Yarantsev D., Plasma-enhanced mixing and flameholding in supersonic flow. Philosophical Transactions of the Royal Society A, 2015, 373(2048): 20140337.

[20] Jin D., Cui W., Li Y., Li F., Jia M., Sun Q., Characteristics of pulsed plasma synthetic jet and its control effect on supersonic flow. Chinese Journal of Aeronautics, 2015, 28(1): 66–76.

[21] Sun Q., Li Y., Cheng B., The characteristics of surface arc plasma and its control effect on supersonic flow. Physics Letters A, 2014, 378(36): 2672–2682.

[22] Zhao G.Y., Li Y.H., Liang H., Phenomenological modeling of nanosecond pulsed surface dielectric barrier discharge plasma actuation for flow control. Acta Physica Sinica, 2015, 64(1): 166–176.

[23] Gan T., Jin D., Guo S., Influence of ambient pressure on the performance of an arc discharge plasma actuator. Contributions to Plasma Physics, 2018, 58(4): 260–268.

[24] Tweedt D.L., Schreiber H.A., Starken H., Experimental investigation of the performance of a supersonic compressor cascade. Journal of Turbomachinery, 1988, 110(4): 456–466.